Synthesis routes of CeO 2 nanoparticles dedicated to organophosphorus degradation: a benchmark

Isabelle Trenque, Greta Camilla Magnano, Jan Bárta, Fréderic Chaput, Marie Alexandrine Bolzinger, Isabelle Pitault, Stéphanie Briançon, Karine Masenelli-Varlot, Matthieu Bugnet, Christophe Dujardin, et al.

Journal Name

ARTICLE TYPE

Cite this: DOI: 00.0000/xxxxxxxxxx

Synthesis routes of CeO_2 nanoparticles dedicated to organophosphorus degradation: a benchmark†

Isabelle Trenque,[abc‡] Greta Camilla Magnano,[a‡] Jan Bárta,[ef‡] Frédéric Chaput,[c] Marie Alexandrine Bolzinger,[a] Isabelle Pitault,[a] Stéphanie Briançon,[a] Karine Masenelli-Varlot,[d] Matthieu Bugnet,[d] Christophe Dujardin,[b] Václav Čuba,[e] David Amans,*[b]

Received Date
Accepted Date

DOI: 00.0000/xxxxxxxxxx

Exposure to organophosphorus compounds, in military conflicts or terrorist acts, requires an emergency procedure including the availability of efficient decontamination system. Systems based on nanosized cerium (IV) oxide (CeO_2) are suitable candidates. CeO_2 is a heterogeneous catalyst for the degradation of the organophosphorus compounds such as VX agent or sarin. While the synthesis method influences the physicochemical characteristics of the nanoparticles surface and thus their degradation activity, we have compared the degradation activity of nanosized CeO_2 powders commercially available, or developed using different synthesis process, namely hydrothermal process, photochemistry, and laser ablation in liquids. The degradation activity was evaluated in vitro by measuring the degradation kinetics of paraoxon organophosphate. A quenching of the degradation activity is observed on the as-produced particles with a surface pollution, especially when organic molecules with carboxylate ion $R-COO^-$ are involved in the synthesis process. In contrast, laser-generated nanoparticles in ultra-pure water show the best activity, while the sample presents the lowest specific surface area. After annealing, almost all samples present a clean surface and the degradation activity is mainly driven by the specific surface area. We then sought to define a figure of merit including the particles activity for the degradation of Paraoxon, the production costs and the production time. Indeed the two last parameters are essential to assess the relevance of each method in view of marketing.

1 Introduction

Exposure to Organophosphorus compounds (OPs) during terrorist attacks and military conflicts requires an emergency procedure including the availability of efficient decontamination system[1]. OPs compounds, highly represented among the Chemical Warfare Agents (CWA) group, mainly enter the body via skin penetration as well as inhalation and ingestion, causing severe injuries and possible death[2,3]. After exposure to organophosphorus toxic agents, the conventional procedure calls for the application of absorbent powders or water rinsing, which makes the skin decontamination possible, but not the OPs degradation. Some solutions combining a rinsing effect and a toxic degradation are also available (such as RSDL lotion, M258 ou M280 kits). They are impregnated sponges or wipes to be applied on small skin surfaces[2,3]. However, they have specific actions, often high pH and are limited to small surfaces. It would be highly beneficial to develop cheap, efficient and easy to handle reactive sorbents[4]. In recent decades, several nanocrystalline metal oxides have been studied for the degradation of chemicals warfare agents (CWA) and their simulants, including CeO_2[4–7], MnO_2[8], MgO[9,10], CaO[11], Al_2O_3[12,13], TiO_2[14], ZnO[15]. These nanomaterials in the form of dry powders are particularly promising systems. They have the advantage of being able to strongly adsorb toxic molecules and rapidly decompose them into less toxic and/or non-toxic compounds. They thus ensure a concomitant displacement and degradation action of the toxic agent. They are called “destructive/reactive sorbents” to distinguish them from conventional adsorbents, such as active carbon, that simply retain chemical compounds, do not alter their structure and therefore do not annihilate their toxicity[6]. The high

[a] LAGEP, UCBL, CNRS UMR5007, F-69622, Villeurbanne, France.
[b] ILM, UCBL, CNRS UMR5306, F-69622, Villeurbanne, France.
E-mail: david.amans@univ-lyon1.fr
[c] Ecole Normale Supérieure de Lyon, Laboratoire de Chimie, CNRS UMR5182, F-69634, Lyon, France.
[d] Univ Lyon, INSA-Lyon, UCBL, MATEIS, UMR CNRS 5510, F-69621, Villeurbanne, France.
[e] Czech Technical University in Prague, Faculty of Nuclear Sciences and Physical Engineering, Břehová 7, Prague 1, Czech Republic
[f] Academy of Sciences of the Czech Republic, Institute of Physics, Cukrovarnická 10, Prague 6, Czech Republic

† Electronic Supplementary Information (ESI) available: [details of any supplementary information available should be included here]. See DOI: 00.0000/00000000.

‡ These authors contributed equally to this work.

specific surface area of the particles increases their sorption capacity allowing the adsorption of the toxic substance[16]. CeO_2 is well known for its catalytic activity and its UV absorbing ability[17,18]. Cerium dioxide nanoparticles have shown exciting potential for fast degradation of Chemical Warfare Agents (CWA), including organophosphorous compounds[5] and organochloride compounds[19]. However, the physicochemical parameters of the CeO_2 powders favouring the CeO_2-catalysed hydrolysis of the organophosphorus compounds remain to be defined. The nature of the reactive sites, as well as the effect of the surface oxidation states of cerium (Ce_3^+/Ce_4^+ ratio) remain open issues[7]. In our previous work[7], we addressed the activity of different crystallographic planes (facets), which offer different reactive sites. Paraoxon (POX) was chosen as a model OP compound, and the kinetics of degradation was evaluated in vitro in aqueous suspension. CeO_2 NPs of different shape such as nano-octahedra, nanocubes, nanorods, and truncated nano-octahedra were selectively obtained using a hydrothermal method. The rate constant of the degradation kinetics normalized by the specific surface area (k/S_{BET}) clearly showed that the surface sites of the {111} facets lead to a higher activity as compared to the ones on the {100} facets. The relative activity between crystal faces was ascribed to (i) the adsorption probability of the toxic substance, assuming the coordination between the phosphoryl oxygen and cerium atoms, and (ii) the surface density of the Ce doublets with a short Ce–Ce distance (0.383 nm), favouring the phosphatase mimetic activity of CeO_2. However, the surface contamination, the surface defects and the specific surface area also have a strong influence on the degradation kinetics and are mainly set by the synthesis route. In our previous study, the morphologies which have shown better activities are the nano-octahedra ($k = 1.08 \times 10^{-2}$ min^{-1}) and the nanorods ($k = 8.00 \times 10^{-3}$ min^{-1}). The nano-octahedra only had {111} facets; this was not the case of the nanorods, which in turn were characterized by the largest amount of defects as well as the largest specific surface area (S_{BET}). However, for each synthesis method, a controlled tuning of the physico-chemical parameters is not always an easy task, or simply not always a possible task. Reaction temperature, concentration of reactants, presence of surfactants etc. can affect those parameters.

In the present work, the issue of the degradation activity is addressed in a systematic and pragmatic approach. While the synthesis process influences the raw degradation activity, i.e. the decay parameter k, which is the relevant parameter for the development of an efficient decontamination system, we have compared different synthesis process of CeO_2. We then sought to define a figure of merit including the particles activity for the degradation of Paraoxon, the production costs and the production time. Indeed the two last parameters are essential to assess the relevance of each method in view of industrial application. In literature, many techniques have been used to obtain CeO_2, including chemical routes such as precipitation[20], microemulsion synthesis[21], sol-gel methods[22], polyvinyl pyrrolidone (PVP) solution route[23], solvothermal processes[7,24,25], photochemistry[26,27] or sonochemical and microwave assisted chemistry[28]; and physical routes such as pulsed laser ablation in liquids[29], mechanical synthesis[30], plasma synthesis[31]. In this study, CeO_2 nanoparticles were elaborated by hydrothermal method (nano-octahedra and nanorods, which have shown the best phosphatase mimetic activity in our previous work), by photochemistry (truncated nano-octahedra), by pulsed laser ablation in liquids (truncated nano-octahedra), and compared to commercial particles (nanopolyedra). The role of the nanoparticles synthesis method on the degradation kinetics of POX was studied in-vitro in an aqueous suspension.

2 Experimental details

2.1 Pulsed laser ablation in liquids

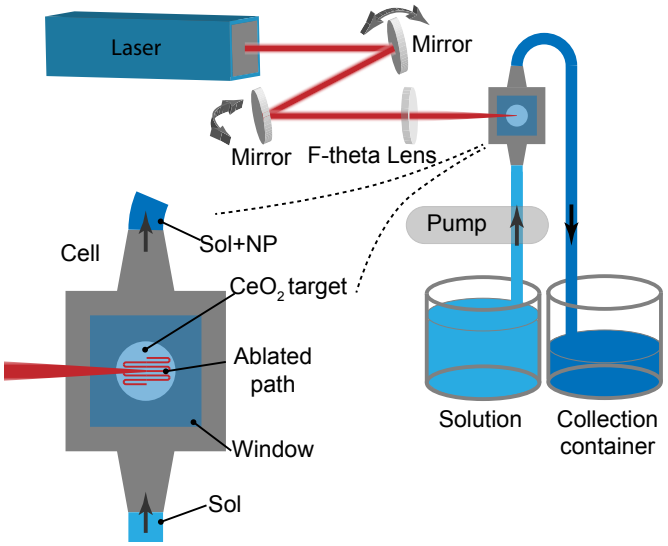

Fig. 1 Schematic representation of the pulsed laser ablation in liquids (PLAL) setup, including the circulation system. A fast steering mirrors system was used to scan the target surface. The ablated surface was 9 mm×12 mm.

Since the 1990s[32], laser ablation in liquids has proven its reliability and its versatility to synthesize nanomaterials in pure water[33–41], including doped nanoparticles and alloys. The nanoparticles are formed during the fast cooling of the laser-generated plasma in the early microseconds following each laser pulse[42]. PLAL provides biocompatible and ligand-free colloids. PLAL can be operated continuously with production rates of several grams per hour[43,44]. Thanks to these advantages, laser-generated nanoparticles are marketed for almost a decade[45].

Nanotruncated octahedra (Φ-NTO) were realized by pulsed laser ablation of a cerium oxide target in ultrapure water (18 MΩ·cm). Targets of pure CeO_2 were sintered pellets made from a commercial micrometer-sized powder of cerium (IV) oxide from Alfa Aesar (Ref. 11327) with a purity of 99.99%. The powder was pressed (0.22 GPa, 3 times for 20 s, 15 s and then 10 s) and then annealed in an oven at 1350°C for 24 h. A circulation system (see figure 1A) was used in order to keep the solvent clear and limit the absorption of the laser beam by the generated nanoparticles. In a typical procedure, the target was placed into a flow cell, whose upper part consists of a glass window, allowing the ablation of the target through it (see figure 1). The flow cell was also connected to ultrapure water source (18 MΩ·cm) with a flow velocity of 5 ml/min. Then, the surface of the tar-

get was irradiated for several hours at room temperature by a Nd:YAG laser (λ = 1064 nm) with a repetition rate of 1 KHz and a pulse duration of 500 ps. The laser source is composed of a passively Q-switched kilohertz Nd:YAG laser amplified with a laser gain module from FiberCryst Company (Taranis module[46]). The energy per pulse was set to 1.8 mJ per pulse. The Gaussian TEM00 beam (beam quality $M^2 < 1.3$) was expanded to reach a $1/e^2$ diameter 2W of 6.5 mm, and was then focused at the surface of the target using a F-Theta lens with 160 mm focal length. The expected beam waist $2W_0$ on the target was then 44 μm. It leads to a surface power density of 2.4×10^{11} W/cm^2. A fast steering mirror system was used to move the laser spot on the surface. The scanning parameters were 5 pulses per spot, 10 μm distance between two spots. After each scan, the laser beam is blocked until the ablation chamber is filled with fresh solution to avoid re-ablation of the particles. It leads to a dead time of 0.9% of the total synthesis duration.

20.4 L of colloidal CeO_2 solution was produced in 68 hours by irradiating successive targets. The measured pH of the colloidal solution was 6.5. This suspension was concentrated with a rotary evaporator (60°C, 120 mbar) to reach a few mL. Finally, the resulting suspension was dried in a drying oven at 60°C for one night in ambient air. 2 g of dried powder was obtained.

2.2 Photochemical ($\chi h\nu$) method

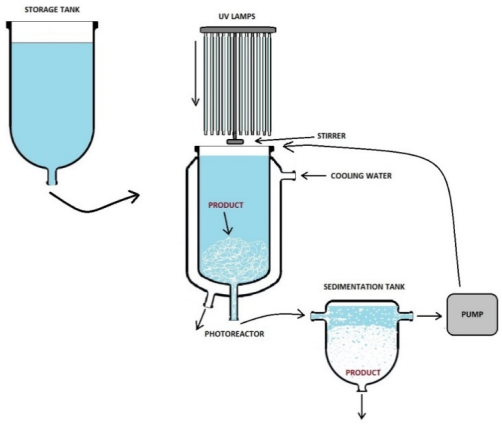

Fig. 2 Photochemical reactor setup (Pilot plant).

UV irradiation of aqueous solutions containing various metal ions (Ag, Rh, Cu, Pb, Ba, Zn, Al ...) and sensitizers, for instance formate $HCOO^-$, is a reliable and efficient method to produce nanoparticles of metal oxides[47–50], including doped particles[51,52] and cerium (IV) oxide[26,27]. A photochemical pilot plant with a reactor of an effective volume of 80 liters has been designed at Czech Technical University to perform large-scale photochemical preparation. The pilot plant is equipped with 28 amalgam low-pressure mercury lamps (44 W, T5Q408-4P-44W from UV Technics) protected by fused silica tubes and immersed into a double-walled photochemical reactor. The reactor was continually cooled by water circulating in the outer layer of the reactor and a coolant unit set to 20°C (hysteresis 1°C).

The synthesis was adapted from Pavelková et al.[27]. Assuming an inner effective volume of 80 liters, the salts were weighted to reach the required concentrations of 5×10^{-3} mol.dm^{-3} cerium nitrate $Ce(NO_3)_3 \cdot 6H_2O$ (173.68 g of cerium nitrate hexahydrate) and 10^{-1} mol.dm^{-3} ammonium formate $HCOONH_4$ (504.48 g). The theoretical yield of CeO_2 from this solution should be 68.8 g. Both salts were weighted separately to prevent precipitation of poorly-soluble cerium formate, and a filling procedure of the reactor has been established. The photochemical reactor was partly filled by deionized water (above 30 liters). Cerium nitrate dissolved in deionized water was then introduced into the reactor by a peristaltic pump. The liquid was stirred for several minutes and diluted by some more deionized water (above 10 liters), after which ammonium formate was added. Just after the introduction of the ammonium formate, no precipitate was observed in the photo-reactor. It was then filled to the top to reach 80 liters and the solution was mixed by stirring and circulation through the sedimentation tank for 30 minutes.

The liquid was then irradiated by the low-pressure mercury lamps for 26 hours. During the process, the solution was vigorously stirred in the inner layer of the photo-reactor. Thanks to the hydrostatic pressure, the irradiated liquid passed into a sedimentation vessel and was then pumped back into the photoreactor by a peristaltic pump (flow≈2 litres per minute). Over the course of irradiation, samples of the solution (10 ml each) were collected and analyzed for the presence of Ce^{3+} ions. For each sample, 5 min centrifugation at RCF 1467 g was performed to separate the synthesized particles from the supernatant containing the remaining Ce^{3+} ions. The analysis consisted in contacting 8 ml of the supernatant with 0.832 ml of a solution containing 0.144 mol.dm^{-3} potassium oxalate (i.e. up to 4×10^{-5} Ce^{3+} + 1.2×10^{-4} ox^{2-}), yielding cerium(III) oxalate precipitate. The cerium oxalate hydrate was then weighed (see Figure S1 in supplementary Information). It appears that the cerium concentration decreased very slowly and the conversion yield to CeO_2 after 26 hours is 38%. The main cause of this effect may be an efficient absorption of UV light by the formed colloidal particles, which did not sediment fully in the sedimentation vessel and were recirculated back to the reactor.

The irradiated solution, along with the brownish particles, was poured out of the pilot plant into two 50-liter barrels, where the formed CeO_2 settled overnight. The gelatinous precipitate composed of the solid product dispersed in liquid was collected and then centrifuged following a recursive protocol. A part of the gelatinous material was centrifuged at RCF 4075 g for 5 min, the supernatant was poured out and another part of the solution was added. In such way, approximately 80 ml of the gelatinous product were separated, containing 26.2 g of CeO_2. The gelatinous product was then dried in a drying oven at 70 °C for 24 hours in ambient air.

2.3 Chemical (χ) method

Cerium oxide nanoparticles were also obtained by a chemical (χ) way. Nanorods (χ-NR), and nano-octahedra (χ-NO) were elaborated by hydrothermal process. The details of the preparation

were described previously[7]. All chemicals were purchased and used without further purification. Cerium nitrate hexahydrate $Ce(NO_3)_3{\cdot}6H_2O$ (Alfa Aesar, 99.5%) was used as the cerium source. To obtain CeO_2 nanorods, 0.03 mol of $Ce(NO_3)_3{\cdot}6H_2O$ dissolved in 100 mL of distilled water was added to 3.6 mol of sodium hydroxide NaOH (Carlo Erba, ACS grade) dissolved in 500 mL of distilled water. After stirring for 20 minutes at room temperature, the solution was transferred into a Teflon-lined stainless steel autoclave and heated at 100°C (1 bar) for 6 hours. To obtain CeO_2 nano-octaedra, 0.0255 mol of $Ce(NO_3)_3{\cdot}6H_2O$ was dissolved in 20 mL of distilled water. This solution was added to a 130 mL solution containing 0.102 mol of ammonium hydroxide NH_4OH (Carlo Erba, ACS grade) at room temperature under strong stirring. After stirring for 20 min, the solution was transferred into a Teflon-lined stainless steel autoclave and heated at 180°C (10.5 bars) for 24 hours. Following the hydrothermal treatment, nanorods and nano-octahedra were cooled at room temperature. Then, fresh precipitates were separated by centrifugation, washed four times with distilled water, and dried in a drying oven at 60°C for one night in ambient air. 5.1 g of nanorods powder were obtained for 13 g of cerium nitrate hexahydrate (one batch, about 100% yield), and 4.4 g of nano-octahedra powder were obtained for 11.1 g of cerium nitrate hexahydrate (one batch, about 100% yield).

2.4 Commercial sample

A commercial suspension (pH 10.2) of nanoparticles with irregular shapes (nanopolyedra, Φ-NPO) was obtained from Baikowski (CTX product). The mass fraction of CeO_2 in the water suspension was 40.4%. The suspension was dried in a drying oven at 60°C for one night in ambient air.

2.5 Annealing post-treatment

A fraction of each synthesized sample was annealed in air at 500°C for two hours. The annealed powders are designated by an asterisk * referring to the annealing post-treatment. Thus, Φ-NPO*, Φ-NTO*, $\chi h\nu$-NTO*, χ-NR* and χ-NO* refer to Φ-NPO, Φ-NTO, $\chi h\nu$-NTO, χ-NR and χ-NO annealed powder respectively.

2.6 Characterization methods

Particle sizes and shapes were observed via transmission electron microscopy (TEM) and high-resolution transmission electron microscopy (HRTEM) on a JEOL 2100 HT apparatus with an accelerating voltage of 200 kV. The TEM samples were prepared by drop-casting onto TEM grids (01844 from Ted Pella, pure carbon film on 400 mesh copper) a droplet of the dispersed powders in water using ultrasonic dispersion. For Φ-NPO sample, characterized by a large polydispersity, the particle size distribution was measured with a Mastersizer 3000 from Malvern based on the technique of laser diffraction. A droplet of the pristine solution was injected in the flow system and the Mie scattering model was used.

Specific surface area was measured by BET method from the N_2 adsorption/desorption isotherms at 77 K using a Belsorp-max instrument.

X-ray diffraction (XRD) patterns were recorded on a Bruker D8 Advance diffractometer equipped with a sealed Cu X-ray tube (40 kV, 40 mA) and a linear Lynxeye XE detector. Data were collected over the range 5-90° with 0.0205° steps. The lattice parameters and the crystallite sizes were extracted from XRD patterns by profile matching (LeBail fit) using the elementary pseudo-Voigt function with the FullProf program packages.

Raman spectra were measured in the range 200-1200 cm^{-1} using a LabRAM Aramis (HORIBA) confocal automated microRaman system with a He-Ne external laser excitation source working at 633 nm and a 50× UV objective. The typical data acquisition time was 5 s. The obtained Raman spectra were normalized relative to the maximum intensity of the F2g mode of the fluorite CeO_2 phase (≈460 cm^{-1}) to allow comparison of the different samples.

The nature of the species adsorbed at the surface of the nanoparticles was studied by infrared spectroscopy on a Perkin-Elmer spectrophotometer (Spectrum 100 FT-IR with universal ATR sampling accessory). The infrared spectra were recorded in the range 550-4000 cm^{-1}. The spectral resolution was 4 cm^{-1}.

2.7 Degradation tests

The protocol for in vitro degradation efficacy of CeO_2 NPs after an exposure to paraoxon (POX) was derived from the protocol described by Salerno et al.[4] with some improvement and was already used in our previous study[7] dealing with the activity of different crystal facets. A solution of 200 μmol/L of POX (0.055 g/L) was prepared in deionized water. For each degradation experiment, 200 mg of CeO_2 was dispersed in 2 mL of the POX solution. A solution of 200 μmol/L of POX, without nanoparticles, was used as a blank.

The samples were taken in glass vials and stirred at 32°C in a water bath under magnetic stirring at 450 rpm for 5 h in order to facilitate interactions between CeO_2 NPs and POX. The degradation of POX was monitored by periodic quantification of POX concentration using High Pressure Liquid Chromatography (HPLC).

Every 30 min, the solution containing nanoparticles was centrifuged at RCF 2292 g for 2 min. 100 μL of supernatant was collected, diluted to 1:10 in deionized water, and filtered through a nylon membrane disc filter (reference Econofltr Nyln 13m, 0.45 μm pore-size) before HPLC analysis. The same procedure has been applied for the blank sample.

HPLC consisted of the quaternary pump (Waters 600 Controller), auto sampler (model 717 plus Auto sampler), column heater (Waters temperature control module), and Photodiode Array Detector (Waters 2996). Operated at 40°C, the column used was a Xterra MS C18 Cartridge column (5 μm, 4.6 mm×250 mm). The composition of the mobile phase was 65% of methanol (HPLC-grade, Fisher Scientific) and 35% of deionized water with 0.5% (v/v) of acetic acid (glacial acetic acid, and ultrapure analytical grade type 1 water, resistivity > 17 MΩ·cm). The flow rate used was 0.7 mL.min^{-1}. The total run time was 10 min and the injection volume was 10 μL. The compound POX was specified by a peak height mode at retention time 7.5 min with UV absorption at λ max 269 nm. The

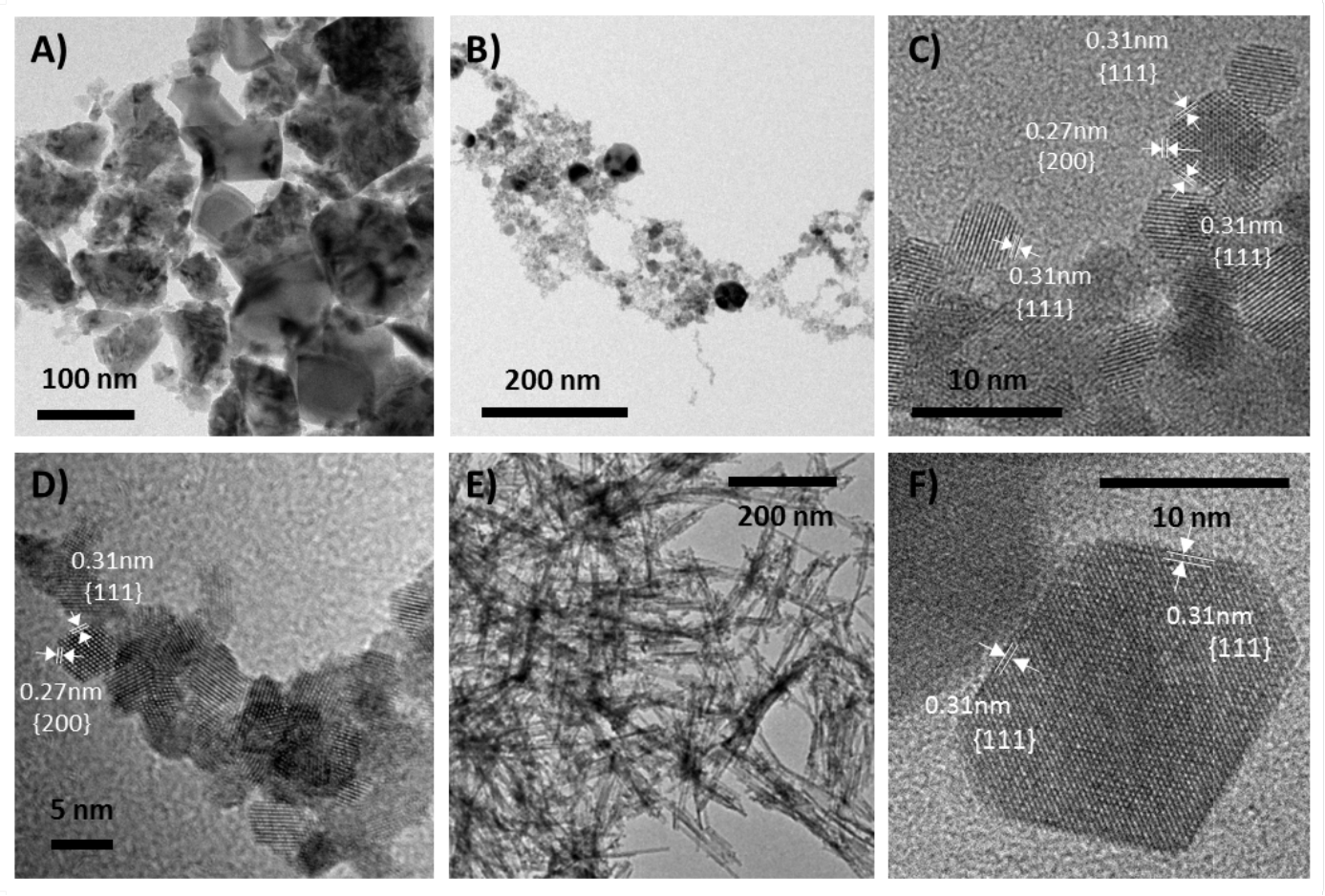

Fig. 3 TEM and HRTEM images of the CeO_2 nanoparticles obtained by both physical and chemical methods. (A) Commercial nanopolyedra Φ-NPO. (B,C) nanotruncated octahedra synthesized by PLAL Φ-NTO. (D) nanotruncated octahedra elaborated by photochemistry $\chi h\nu$-NTO. (E) nanorods χ-NR and (F) nano-octahedra χ-NO elaborated by hydrothermal process.

Table 1 {hkl} Crystal facets, sizes estimated from TEM images, specific surface area S_{BET} of the nanoparticles elaborated by physical and chemical methods before annealing, and $S^{\star}_{\mathrm{BET}}$ after annealing. The size evolution from as-produced particles to annealed particles is displayed only when significant.

Sample	Crystal facets	Sizes from TEM (nm) before → after annealing	$S_{\mathrm{BET}} \rightarrow S^{\star}_{\mathrm{BET}}$ ($m^2.g^{-1}$)
Φ-NTO / Φ-NTO*	{111} + {100}	4 nm for the truncated octahedra and $10-50$ nm for the spheres	$13 \rightarrow 16$
χ-NO / χ-NO*	{111}	$6-35$ nm	$67 \rightarrow 60$
χ-NR / χ-NR*	not selective	$7-9$ nm in diameter $\times$ $50-200$ nm long	$133 \rightarrow 90$
$\chi h\nu$-NTO / $\chi h\nu$-NTO*	{111} + {100}	$4-5$ nm $\rightarrow$ $6-11$ nm	$145 \rightarrow 45$
Φ-NPO / Φ-NPO*	not selective	few nm to few hundred nm	$20 \rightarrow 20$

calibration curve of POX was linear in the concentration range of 0–50 μmol.L^{-1} (according to the dilution, a maximum of 20 μmol.L^{-1} is expected). Data collection and analysis were performed using the Empower Pro software. Under these conditions, the limit of detection of POX was 420 pg. This value corresponds to a minimum concentration of 4.2×10^{-5} g.L^{-1} in the 10 μL injected, i.e. to the residual concentration after removal of 99.2% of POX. The coefficients of variation of repeatability were 0.5% at a concentration level 10 mg.L^{-1} (36 μmol.L^{-1}).

3 Results

Morphological studies The morphology of nanoparticles synthesized by both physical and chemical processes was carried out by transmission electron microscopy (TEM) and high resolution transmission electron microscopy (HRTEM). Figure 3 shows images of the as-produced nanoparticles, before the annealing treatment. All the interplanar distances and angles between crystallographic planes fit those reported in the ICDD file 00-034-0394 corresponding to cubic cerium dioxide (space group 225, $Fm\bar{3}m$). The process used by Baikowski led to the formation of Φ-NPO cerium oxide particles with a very large particle size distribution, from a few nm to a few hundred nm, and irregular shapes (Figure 3A). Because of these irregularities, it was not possible to determine crystal faces for Φ-NPO. Figure S2 in supplementary Information shows the volume-weighted size distribution delivered by the Mastersizer 3000 particle size analyzer, confirming

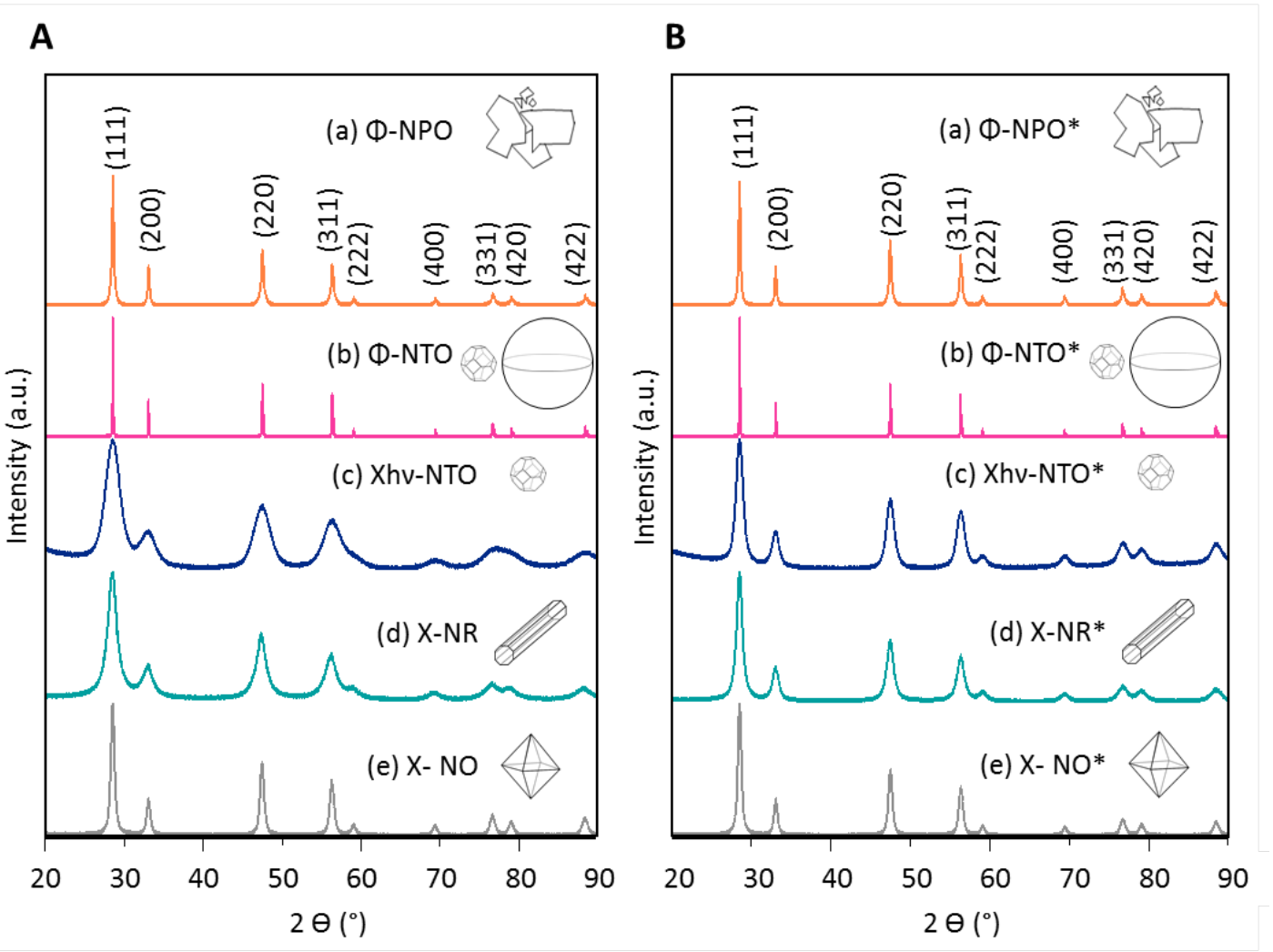

Fig. 4 XRD patterns of the CeO_2 nanoparticles elaborated by physical and chemical methods: (A) as-prepared samples, (B) samples after annealing treatment.

Table 2 Refined lattice parameter *a*, refined crystallite size and relative intensity ratio I_D/I_{F2g} of the samples before and after annealing treatment. Lattice parameters and crystallite size were extracted from profile refinements on the X-Ray diffractograms, using the Fullprof software. Rp and Rwp are respectively profile and weighted profile reliability factors. The fit is considered reliable when Rp and Rwp are below 10%. No values of the crystallite size were extracted for Φ-NTO and for Φ-NTO*, because it was not possible to distinguish the contribution of each population of particles. I_D/I_{F2g} ratios were determined from Raman spectra.

Sample	a (Å)	Crystallite size (nm)	Rp (%)	Rwp (%)	I_D/I_{F2g}
Φ-NTO	5.411(2)	–	6.74	9.93	0.27
χ-NO	5.416(1)	15	3.42	5.47	0.62
χ-NR	5.431(3)	6	4.57	5.92	4.11
χ*hν*-NTO	5.43(2)	3	10.7	9.1	6.19
Φ-NPO	5.411(2)	38	7.12	9.43	0.68
Φ-NTO*	5.411(1)	–	6.01	9	0.25
χ-NO*	5.414(1)	15	3.43	5.69	0.58
χ-NR*	5.413(1)	10	3.75	5.45	1.11
χ*hν*-NTO*	5.403(7)	8	10.8	9.45	1.45
Φ-NPO*	5.411(1)	47	5.72	8.05	0.81

the broad size distribution. By using pulsed laser ablation in ultrapure water, two types of particles were obtained for Φ-NTO: a majority of nanotruncated octahedra of approximatively 4 nm, and some spherical nanoparticles between 10 nm and 50 nm (Figure 3B,C). The nanotruncated octahedra present {111} and {100} crystal facets. By using photochemistry synthesis, only nanotruncated octahedra of approximatively 4 nm were obtained, with {111} and {100} crystal facets at their surface (Figure 3D). By using the hydrothermal process, nanorods and nano-octahedra were obtained (Figure 3E-F). The morphologic details of these samples are described in our previous study[7]. Briefly, the χ-NR (Figure 3E) consist of rods about 7-9 nm in diameter and 50-200 nm long, which grew along the $< 110 >$ direction. They are porous, polycrystalline and don't present well defined facets. The χ-NO (Figure 3F) have sizes ranging between 6 nm and 35 nm. They are in an octahedron shape with truncation at the apexes and their surface is dominated by {111} crystal facets. All the morphologic characteristics of the nanoparticles are reported in Table 1 along with their specific surface areas.

The morphology of the annealed nanoparticles was also studied. HTEM images, TEM images and the report of morphological characteristics of the annealed nanoparticles are presented in supplementary information (see Figure S3). No significant modification of the morphology was observed with the annealing treatment except for nanotruncated octahedra prepared by photochemical synthesis and for nanorods. In the case of nanotruncated octahedra prepared by photochemical synthesis, the annealing treatment induces the sintering of the nanoparticles and an increase in size from 4-5 nm to 6-11 nm. This leads to a decrease of the specific area (145 $m^2.g^{-1}$ for $\chi h\nu$-NTO, 45 $m^2.g^{-1}$ for $\chi h\nu$-NTO*). In the case of nanorods, the annealing treatment did not affect the size or the shape, but a decrease of the specific surface area was noticed after the annealing (132.5 $m^2.g^{-1}$ for χ-NR, 90 $m^2.g^{-1}$ for χ-NR*). An explanation could be a decrease of the porosity of the objects with the annealing treatment.

Phase determination and structural refinements The crystal structure of the nanoparticles was characterized by XRD analysis. The XRD patterns of the as-prepared nanoparticles are presented in Figure 4A. All the diffraction patterns present only reflections characteristic of the cubic fluorite structure of cerium dioxide (ICDD 00-034-0394, space group 225, $Fm\bar{3}m$). The nature of the crystalline phase was not affected by the annealing treatment (Figure 4B). The lattice parameters and the crystallite size of the different samples, before and after annealing, determined from profile matching refinements, are reported in Table 2. Except for $\chi h\nu$-NTO and χ-NR, the lattice parameter of the as-prepared nanoparticles is slightly higher than –, although quite close to – the value of the lattice parameter of bulk CeO_2 (5.411 Å), consistently with the Madelung constant in an ionic crystal of CeO_2 [53,54]. For χ-NR and $\chi h\nu$-NTO, a higher value of the lattice parameter is observed, about 5.43 Å. The distortion of the crystal lattice of the nanorods χ-NR has been previously attributed to the strain induced by twist boundaries, as well as by the presence of Frenkel-type oxygen defects [7]. After the annealing, the lattice parameter of the nanorods χ-NR* as well as of the nanotruncated octahedra $\chi h\nu$-NTO* is moving toward the bulk value, showing that the strain is considerably reduced by the annealing step. This is consistent with the increase of the crystallite size.

Raman spectroscopy The Raman spectra of the CeO_2 nanoparticles before and after the annealing treatment in the 350–700 cm^{-1} range are shown in Figure 5. The full spectra are available in supplementary information, figure S4. For all samples, the Raman spectrum is dominated by a strong peak at ≈460 cm^{-1}, with weak bands at ≈600 cm^{-1}. The peak at ≈460 cm^{-1} (labelled F_{2g}) is typical for the CeO_2 fluorite phase, and corresponds to a symmetric breathing mode of the oxygen atoms around cerium ions. This mode is affected by any disorder in the sublattice, and is size dependent [55,56]. Thus, it is not surprising that the presence of twist boundary or of other structural defects in χ-NR or in $\chi h\nu$-NTO involve a redshift, and a broadening of the F_{2g} peak compared to other morphologies (Figure 5). The peak around 600 cm^{-1} (labelled D) is assigned to oxygen defects, and most probably due to the presence of Frenkel-type oxygen defects where an oxygen atom is displaced from its lattice position to an interstitial site [57,58].

The relative intensity ratio I_D/I_{F2g} gives information about the quantity of intrinsic defect sites in the structure. The I_D/I_{F2g} ratio of the different samples is reported in Table 2. Before the annealing, the I_D/I_{F2g} ratio of $\chi h\nu$-NTO and χ-NR is more than six times higher than the values of the other samples (Figure 5A,B and Table 2), indicating that $\chi h\nu$-NTO and χ-NR have the largest quantity of Frenkel-type oxygen defects. The I_D/I_{F2g} ratio is not significantly affected by the annealing treatment, except for the nanotruncated octahedra elaborated by photochemistry and for the nanorods (Figure 5C,D and Table 2). The I_D/I_{F2g} of $\chi h\nu$-NTO* and χ-NR* is reduced by a factor four with respect to the values of the as-produced samples. This result is consistent with an annealing in presence of oxygen (in air) which is expected to induce a decrease of oxygen defects. The results from Raman and XRD are then consistent. A large amount of Frenkel-type oxygen defects leads to an increase of the lattice parameter, and both are reduced by the annealing treatment.

Nature of the adsorbed species The nature of the adsorbed species at the surface of the CeO_2 nanoparticles was characterized by infrared spectroscopy. Figure 6 shows IR spectra of the different samples before and after the annealing step. The assignment of the peaks is detailed in the supplementary information (Table S1). In the following, we focus on the main information provided by the IR spectroscopy.

Before heat treatment the infrared spectra have different absorption bands according to the approach used for the synthesis. Thus, for the powders resulting from syntheses in autoclave (χ-NR and χ-NO), the following bands are observed: 3400, 1630, 1540, 1330, 1050, 850, 710 cm^{-1}. The first two bands are due to adsorbed water molecules and OH surface groups. The rest of the bands are assigned to carbonates interacting with basic surface lattice oxygen. The carbonates thus bonded exhibit different modes of interaction: Monodentate, Bidentate and Polydentate. The last two are the most likely, in view of the position of the bands [59,60]. For these two ceria nanopowders, the shape of the spectra was slightly affected by the post-annealing treatment.

For Φ-NPO and $\chi h\nu$-NTO nanoparticles, bands are very slightly visible around 2900 cm^{-1}, which are characteristics of C-H stretching. For the $\chi h\nu$-NTO sample, this band and the two strong COO bands (above 1550 cm^{-1} and 1350 cm^{-1}) are a manifestation of the formate ions $HCOO^-$ used as sensitizers in the photochemical synthesis. For Φ-NPO sample, the same bands are probably a signature of ligands used to stabilize the colloidal CeO_2 suspension. In both case, molecules used in the synthesis protocols lead to an important pollution of the nanoparticles surface, but the annealing step leads to their degradation: for $\chi h\nu$-NTO* nanoparticles, the C-H peak (above 2900 cm^{-1}) and the COO bands (1600-1200 cm^{-1} range) disappear with the annealing step; while they are reduced for Φ-NPO*.

For PLAL-synthesized nanoparticles, the peaks at 1100 cm^{-1} (ν(CO)) and 1262 cm^{-1} (δ(COH)) observed on the FTIR spectrum of the as-produced sample are characteristic of the presence of hydrogen carbonate at the surface of the particles [60], probably

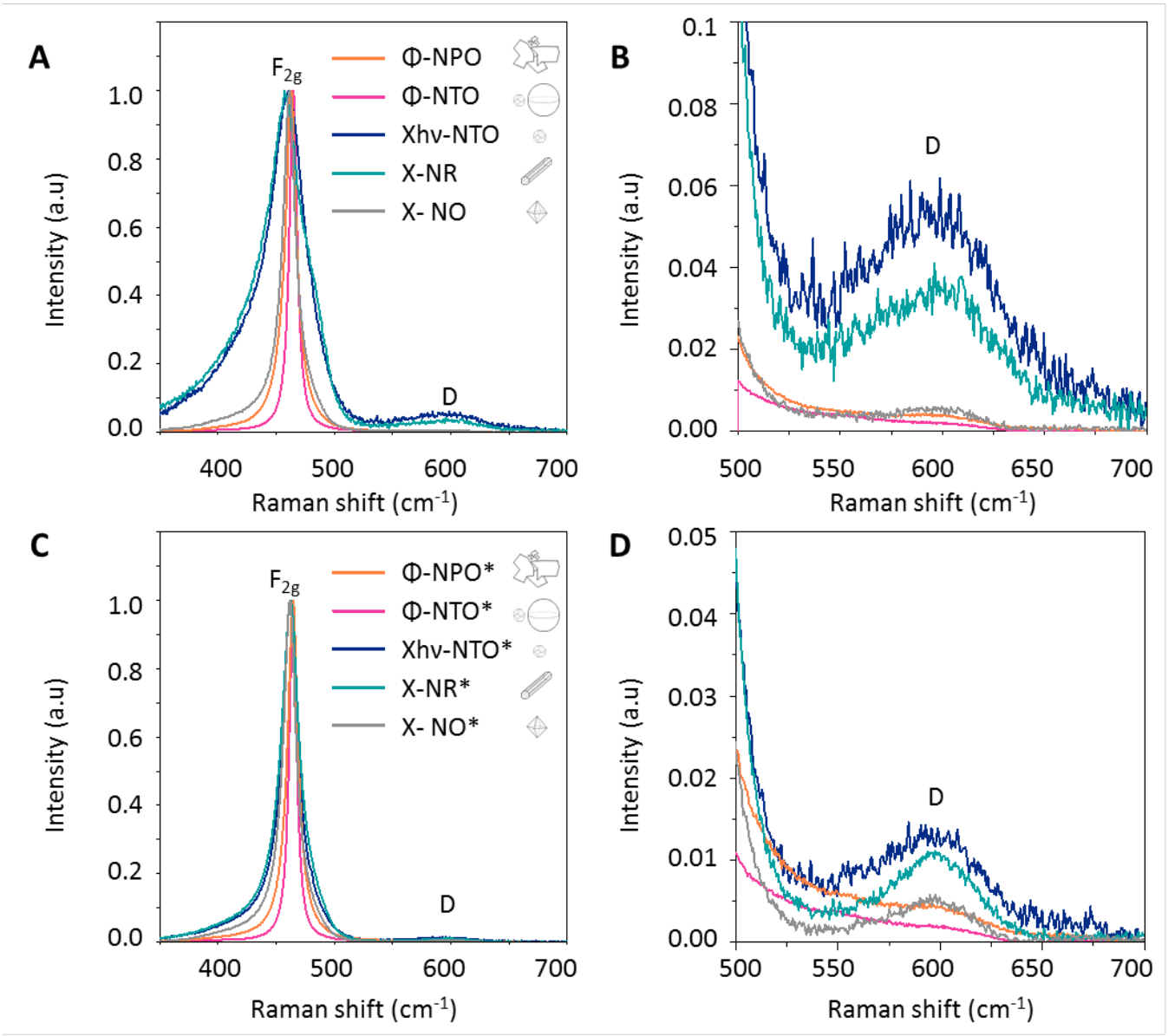

Fig. 5 Raman spectra of the cerium oxide nanoparticles before (A,B) and after (C,D) the annealing treatment. (A,C) Raman spectra in the 350-700 cm^{-1} range and (B,D) enlarging in the 500-700 cm^{-1} range ($\lambda_{exc} = 633$ nm). All spectra are normalized relative to the maximum intensity of the F_{2g} mode of the CeO_2 fluorite phase.

originating from dissolved CO_2. The pH value of the colloidal solution is 6.5 and is thus consistent with the presence of hydrogen carbonate ($pKa_1 = 6.4$ for H_2CO_3 / HCO_3^- and $pKa_2 = 10.3$ for HCO_3^- / CO_3^{2-}). Both hydrogen carbonate signature are not observed on Φ-NTO*.

Finally, for all cerium oxide nanopowders, the strong band below ≈600 cm^{-1} corresponds to O-Ce-O vibration of cerium oxide.

Degradation activity The degradation of paraoxon using the as-produced particles as well as after their annealing is shown in Figure 7. The in vitro method used for the test gives information about the degradation efficiency of the particles in aqueous phase at 32°C. The as-produced particles (Figure 7A) can be classified in two groups based on the kinetic of degradation. The first group causes the degradation of approximatively 40% of the initial POX in 1 hour and of almost all initial POX in 5 hours. The second group allows the degradation of less than 10% of initial POX in 1 hour and around 30% of initial POX in 5 hours. The first group is constituted of Φ-NTO, χ-NO and χ-NR, and the second group is constituted of $\chi h\nu$-NTO and Φ-NPO. After the annealing treatment (Figure 7B), some important modifications were observed : 1) an increase of the degradation efficiency for the nanorods prepared by hydrothermal process, for the nanotruncated octahedral particles synthesized by photochemistry and for the nanopolyhedra produced by wet grinding, 2) a decrease of the degradation efficiency for the nanotruncated octahedra elaborated by PLAL. The kinetics of the nano-octahedra prepared by hydrothermal process did not seem to be affected by the annealing treatment. The evolution of paraoxon degradation with time

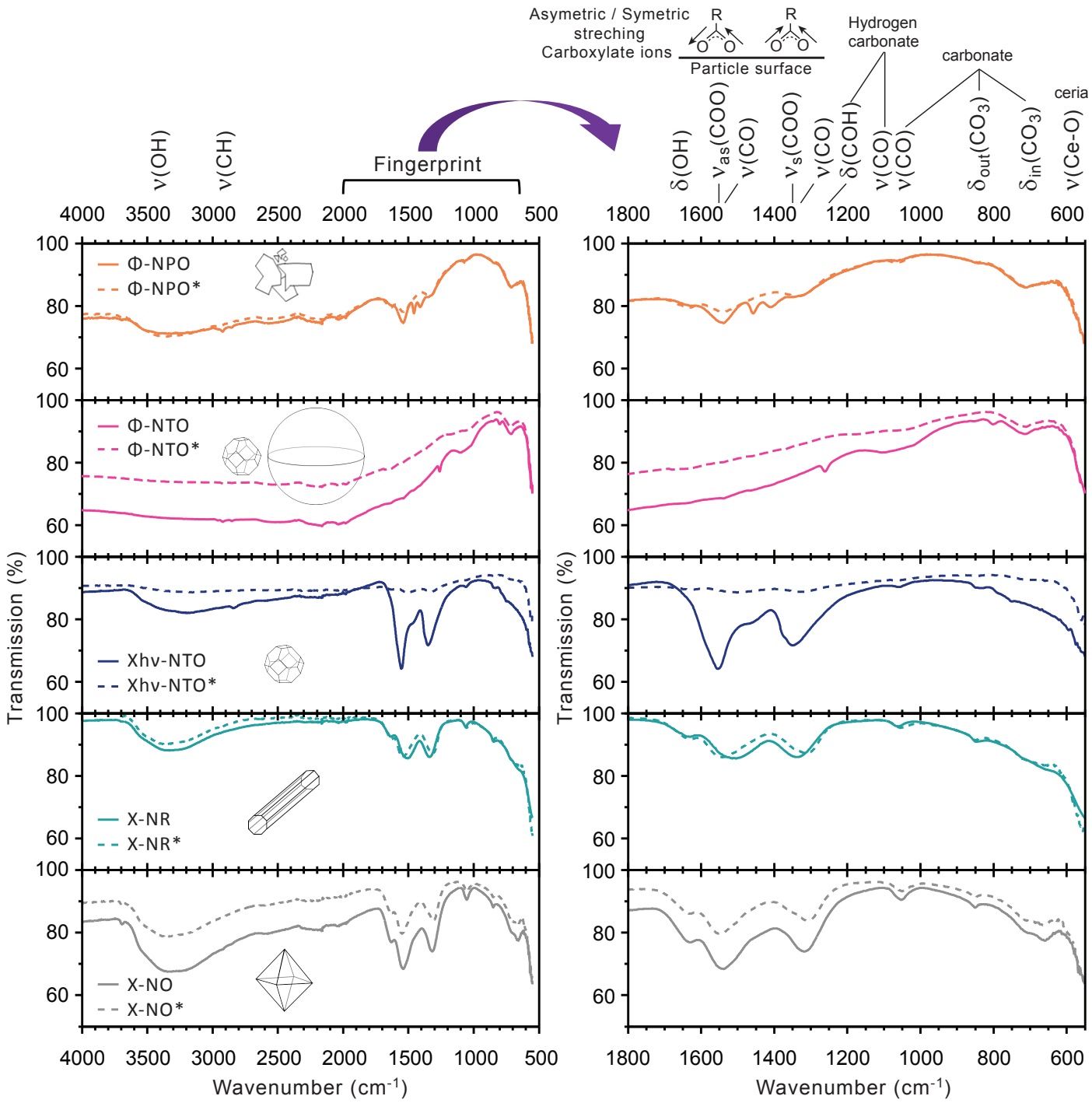

Fig. 6 IR spectra of all the cerium oxide nanoparticles (A) in the 4000-500 cm^{-1} range and (B) enlarging in the 1800-550 cm^{-1} range. As-produced samples (before annealing) are displayed with a continuous line. Sample after the annealing treatment are represented with a dotted line. Symbol ν and δ represent the stretching vibration and the bending vibration respectively. δ_{out} names a bending out-of-plan, δ_{in} a bending in-plane, ν_{as} an asymmetric stretching, and ν_s a symmetric stretching.

after contact with CeO_2 samples was fitted with a pseudo-first order decay model (exponential decay $\propto \exp(-kt)$, with a rate constant k (min^{-1}). The detailed values of the rate constant k and the rate constant normalized by the specific surface area k/S_{BET} are reported in Table 3.

4 Discussion

The degradation activity of the samples before the annealing step is driven by the surface pollution. The two samples with a poor degradation activity, namely $\chi h\nu$-NTO and Φ-NPO are characterized by synthesis processes which lead to a pollution of the surface of the nanoparticles, formate ions for $\chi h\nu$-NTO and ligands for Φ-NPO respectively, while $\chi h\nu$-NTO presents the largest

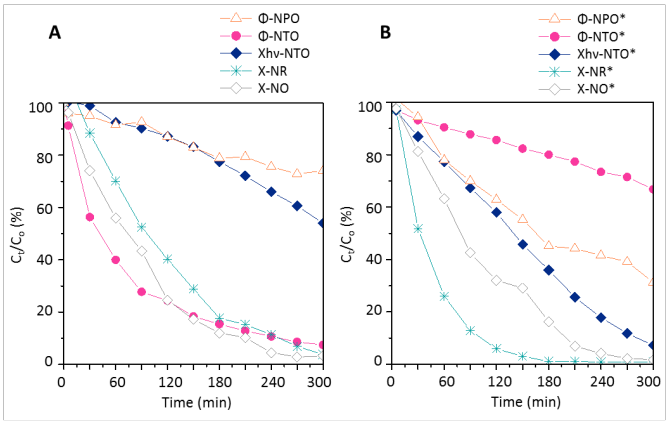

Fig. 7 Degradation kinetic of Paraoxon with the CeO_2 nanoparticles: (A) as-prepared samples, (B) samples after annealing treatment.

Table 3 Parameters extracted from the degradation kinetics of Paraoxon for the different samples. k and k/S_{BET} are respectively the rate constant and the rate constant normalized by the specific surface area of the considered sample, $t_{1/2} = \ln(2)/k$ is the resulting half-life of the degradation kinetics, R^2 is the reliability factor of the pseudo-first order decay function used for the fit of the degradation kinetics. The asterisks $\star$ denote the annealed samples.

Sample	k (min^{-1})	$t_{1/2}$ (min)	R^2	k/S_{BET} ($g.m^{-2}.min^{-1}$)
Φ-NTO	1.30×10^{-2}	53	0.966	9.14×10^{-4}
χ-NO	1.08×10^{-2}	64	0.994	1.62×10^{-4}
χ-NR	8.00×10^{-3}	87	0.973	6.04×10^{-5}
χ$h\nu$-NTO	1.64×10^{-3}	423	0.941	1.13×10^{-5}
Φ-NPO	1.14×10^{-3}	608	0.956	5.67×10^{-5}
Φ-NTO*	1.30×10^{-3}	535	0.980	8.00×10^{-5}
χ-NO*	9.52×10^{-3}	73	0.984	1.58×10^{-4}
χ-NR*	2.20×10^{-2}	31	0.996	2.44×10^{-4}
χ$h\nu$-NTO*	5.85×10^{-3}	119	0.963	1.30×10^{-4}
Φ-NPO*	3.85×10^{-3}	180	0.988	1.92×10^{-4}

specific surface area, 145 $m^2.g^{-1}$ (see table 1). In contrast, laser-generated nanoparticles in ultra-pure water Φ-NTO show the best activity, while this sample presents the worst specific surface area, 13 $m^2.g^{-1}$ (see table 1).

After the annealing, the degradation activity is mainly driven by the specific surface area: the larger is the specific surface area, the higher is the rate constant k. All samples present different facets, at least {111} and {100}, including the so called nano-octahedra χ-NO and χ-NO* which appear slightly truncated. Then, despite the higher activity of the {111} facets with respect to the {100} facets[7], the shape of particles appears as a second order effects with respect to the specific surface area for the annealed samples, keeping in mind that all samples present a large amount of {111} facets. The values of the ratio k/S_{BET} for the annealed samples are similar, $1.6 \pm 0.8 \times 10^{-4}$ $g.m^{-2}.min^{-1}$.

5 Benchmarking of degradation activity, costs and productivity

To compare the different synthesis methods, we have sought to assess the pros and cons of each of them through the definition of relevant quantities, i.e. the productivity (g/day), the hourly production rate (mg/h), the costs (€/g) and the rate constant k (min^{-1}). The values are displayed in table 4 for the samples with the highest rate constant k for each synthesis method, i.e. the as-produced sample or the annealed sample. The commercial sample is excluded since the information on costs, the productivity and the hourly production rate are confidential.

Table 4 Rate constant k of paraoxon degradation, productivity, costs and hourly production rate. The table presents the samples with the best rate constant k for each synthesis method, i.e. the as-produced sample or the annealed sample. The commercial sample is excluded since the information on costs, the productivity and the hourly production rate are confidential.

Sample	$k \times 10^{-3}$ (min^{-1})	Productivity (g/Day)	costs (€/g)	hourly production rate (mg/h)
Φ-NTO	13.0	0.25	986.21	21
χ-NO	10.8	34.33	6.61	1925
χ-NR*	22.0	15.50	14.62	873
χ$h\nu$-NTO*	3.85	13.10	21.73	481

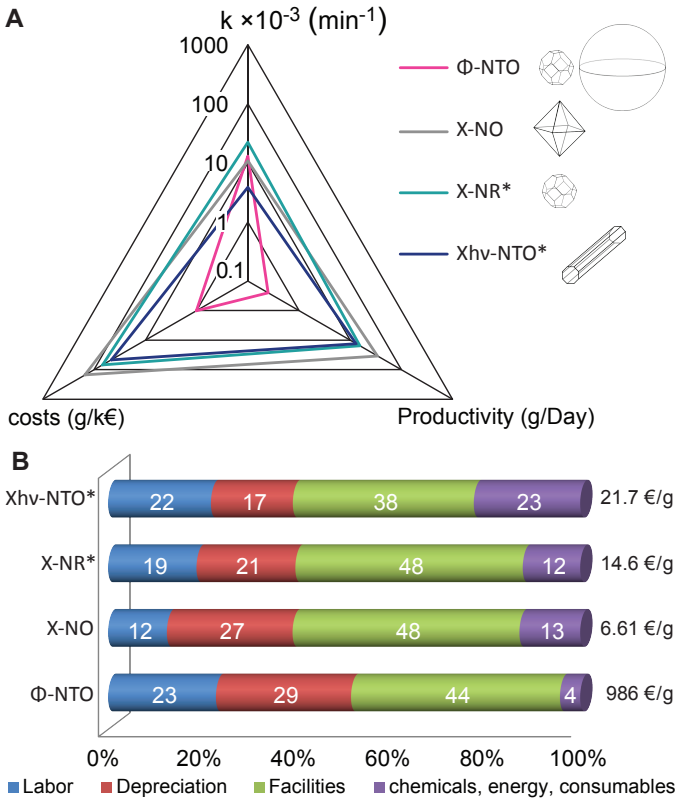

Fig. 8 (A) Comparison of the degradation activity, costs and productivity. (B) Cost breakdown including labor, depreciation of the investments (equipment), the rental cost of the facilities, and the energy costs, the chemicals and the consumables.

The costs include labor costs (26.14 €per working hour for an operator including taxes, 1607 working hours per years), the depreciation of the investment (equipment) assuming a depreciation time of five years (1760 hours of useful machine time per year), the rental cost of the facilities (109 €per working day for an experimental room of 30 m^2, including a fume hood, the processing of the chemical waste, fluids consumption, air conditioning, cleaning, building maintenance and security), the energy costs

(0.12 €/kWh VAT excluded), the chemicals (VAT excluded) and the lab consumables (VAT excluded). Research and development costs, as well as the quality control are not included, but would be similar for all synthesis methods. The detail of the calculation is available in supplementary information (Excel file).

The productivity (g/day) for each method, assuming a continuous process and a parallelization of the production steps, is driven by the step in the production process with the longest operating times. The productivity is thus driven by the immobilization of critical equipment, including its cleaning and/or cooling times. It corresponds to the laser setup for the PLAL method, the autoclave for the hydrothermal process, and the photochemical reactor for the photochemical method. The hourly production rate corresponds to the weight of dried powder produced in one batch divided by the overall time to release one batch (mg/h). The productivity (g/day) and the hourly production rate (mg/h) are complementary information. The facilities costs mainly relied on the productivity, while the labor and the depreciation mainly relied on the hourly production rate.

It appears from table 4 and figure 8 that the hydrothermal process is slightly less expensive than the photochemical method, and both of them are substantially less expensive than laser ablation in liquids. Moreover, the hydrothermal process leads to the powders with the best degradation activity, namely the nanorods. PLAL is penalized by the low productivity which results mechanically in a rise of the costs, including labor costs, the depreciation of the investment and the facilities costs. However, a drastic rise of the productivity, from 21 mg/hour (overall process) to a few g/hour is possible with available laser sources[43,44]. For productivity larger than a few g/hour, laser ablation in liquids would compete with the chemical routes[61], keeping in mind that as-produced sample from PLAL exhibits one of the best degradation activity. The Photochemical method is penalized by the conversion yield obtained, only 38%, limiting the amount of particles produced in one batch, which results mechanically in a rise of the costs. In contrast the conversion yield reported for the hydrothermal process is 100%. An increase of the conversion yield by means of an optimization of the photochemical method (in-line filtering, forced sedimentation etc.) would leads to reduced costs which may reach 8.26 €/g for an ideal conversion yield of 100%, i.e. in the range of the hydrothermal method costs.

6 Conclusions

The degradation activity of CeO_2 nanopowders was evaluated in vitro by measuring the degradation kinetics of paraoxon organophosphate. The degradation activity of the as-produced nanopowders is strongly influence by the synthesis route. A quenching of the degradation activity is observed on the as-produced particles with a surface pollution, especially when organic molecules with carboxylate ion $R-COO^-$ are involved in the synthesis process. In contrast, laser-generated nanoparticles in ultra-pure water show the best activity, while the sample presents the lowest specific surface area. After annealing, almost all samples present a clean surface and the degradation activity is mainly driven by the specific surface area. The benchmarking of costs and productivity shows that the costs are mainly driven by the productivity, disadvantaging the laser ablation in liquids with respect to the chemical and the photochemical routes. However, such a drawback is solved by cutting edge device allowing an ablation rate of a least one gram per hour. For now, chemical routes remain the least expensive while leading to the nanoparticles with the best degradation activity of the paraoxon, namely the nanorods.

Conflicts of interest

There are no conflicts to declare.

Acknowledgements

The authors are thankful to Ruben Vera for carrying out the XRD measurements. This work received financial support from the Direction Générale de l'Armement (PhD grant), and from the DGA ASTRID program (project NanoDeTox – Grant no. ANR-16-ASTR-0008). The collaboration between the Lyon University and the Institute of Physics of the Czech Academy of Sciences is funded through the European project ASCIMAT, in the framework of the European program H2020-TWINN-2015. The pilot plant experiments were supported by the Ministry of Industry and Trade of the Czech Republic project FV30139. We wish to thank Fibercryst company for the custom-development of the MOPA-based laser source, as well as for their technical support. The ablation setup was funded by the French innovation agency OSEO *ALL-Mat* project. We wish to thank BAIKOWSKI for providing us ceria suspension (CTX product).

Notes and references

1 N. Sharma and R. Kakkar, *Adv. Mater. Lett.*, 2013, **4**, 508–521.
2 K. Kim, O. G. Tsay, D. A. Atwood and D. G. Churchill, *Chem. Rev.*, 2011, **111**, 5345–5403.
3 Y. J. Jang, K. Kim, O. G. Tsay, D. A. Atwood and D. G. Churchill, *Chem. Rev.*, 2015, **115**, PR1–PR76.
4 A. Salerno, T. Devers, M.-A. Bolzinger, J. Pelletier, D. Josse and S. Briancon, *Chem.-Biol. Interact.*, 2017, **267**, 57–66.
5 P. Janos, P. Kuran, M. Kormunda, V. Stengl, T. M. Grygar, M. Dosek, M. Stastny, J. Ederer, V. Pilarova and L. Vrtoch, *Journal of Rare Earths*, 2014, **32**, 360 – 370.
6 P. Janoš, J. Henych, O. Pelant, V. Pilařová, L. Vrtoch, M. Kormunda, K. Mazanec and V. Štengl, *J. Hazard. Mater.*, 2016, **304**, 259–268.
7 I. Trenque, G. C. Magnano, M. A. Bolzinger, L. Roiban, F. Chaput, I. Pitault, S. Briancon, T. Devers, K. Masenelli-Varlot, M. Bugnet and D. Amans, *Phys. Chem. Chem. Phys.*, 2019, **21**, 5455–5465.
8 X. Liao, C. Zhang, Y. Liu, Y. Luo, S. Wu, S. Yuan and Z. Zhu, *Chemosphere*, 2016, **150**, 90–96.
9 G. Wagner, P. Bartram, O. Koper and K. Klabunde, *J. Phys. Chem. B*, 1999, **103**, 3225–3228.
10 A. Sellik, T. Pollet, L. Ouvry, S. Briancon, H. Fessi, D. J. Hartmann and F. N. R. Renaud, *Chem.-Biol. Interact.*, 2017, **267**, 67–73.
11 G. Wagner, O. Koper, E. Lucas, S. Decker and K. Klabunde, *J. Phys. Chem. B*, 2000, **104**, 5118–5123.

12 G. K. Prasad, P. V. R. K. Ramacharyulu, K. Batra, B. Singh, A. R. Srivastava, K. Ganesan and R. Vijayaraghavan, *J. Hazard. Mater.*, 2010, **183**, 847–852.

13 G. Wagner, L. Procell, R. O'Connor, S. Munavalli, C. Carnes, P. Kapoor and K. Klabunde, *J. Am. Chem. Soc.*, 2001, **123**, 1636–1644.

14 G. W. Wagner, Q. Chen and Y. Wu, *J. Phys. Chem. C*, 2008, **112**, 11901–11906.

15 T. H. Mahato, G. K. Prasad, B. Singh, J. Acharya, A. R. Srivastava and R. Vijayaraghavan, *J. Hazardous Materials*, 2009, **165**, 928–932.

16 G. Wagner and Y. Yang, *Ind. Eng. Chem. Res.*, 2002, **41**, 1925–1928.

17 A. Trovarelli, C. de Leitenburg, M. Boaro and G. Dolcetti, *Catalysis Today*, 1999, **50**, 353 – 367.

18 Y. Ma, W. Gao, Z. Zhang, S. Zhang, Z. Tian, Y. Liu, J. C. Ho and Y. Qu, *Surf. Sci. Rep.*, 2018, **73**, 1–36.

19 W. Chen, R. Ran, D. Weng, X. Wu, J. Zhong and S. Han, *Journal of Rare Earths*, 2017, **35**, 970 – 976.

20 H. Chang and H. Chen, *J. Cryst. Growth*, 2005, **283**, 457–468.

21 C. Tiseanu, V. I. Parvulescu, M. Boutonnet, B. Cojocaru, P. A. Primus, C. M. Teodorescu, C. Solans and M. Sanchez Dominguez, *Phys. Chem. Chem. Phys.*, 2011, **13**, 17135–17145.

22 T. Yu, J. Joo, Y. Park and T. Hyeon, *Angew. Chem.-Int. Edit.*, 2005, **44**, 7411–7414.

23 S. Phoka, P. Laokul, E. Swatsitang, V. Promarak, S. Seraphin and S. Maensiri, *Mater. Chem. Phys.*, 2009, **115**, 423–428.

24 H. Mai, L. Sun, Y. Zhang, R. Si, W. Feng, H. Zhang, H. Liu and C. Yan, *J. Phys. Chem. B*, 2005, **109**, 24380–24385.

25 K. Wang, H. Niu, J. Chen, J. Song, C. Mao, S. Zhang, S. Zheng, B. Liu and C. Chen, *Materials*, 2016, **9**, 326–337.

26 K. Kamada, K. Horiguchi, T. Hyodo and Y. Shimizu, *Cryst. Growth Des.*, 2011, **11**, 1202–1207.

27 T. Pavelkova, V. Vanecek, I. Jakubec and V. Cuba, *Radiat. Phys. Chem.*, 2016, **124**, 252–257.

28 H. Wang, J. Zhu, J. Zhu, X. Liao, S. Xu, T. Ding and H. Chen, *Phys. Chem. Chem. Phys.*, 2002, **4**, 3794–3799.

29 Y. Takeda and F. Mafune, *Chem. Phys. Lett.*, 2014, **599**, 110–115.

30 Y. X. Li, X. Z. Zhou, Y. Wang and X. Z. You, *Materials Letters*, 2004, **58**, 245 – 249.

31 M. Davoodbasha, B.-R. Park, W.-J. Rhee, S.-Y. Lee and J.-W. Kim, *Arch. Biochem. Biophys.*, 2018, **645**, 42–49.

32 D. Amans, W. Cai and S. Barcikowski, *Appl. Surf. Sci.*, 2019, **488**, 445–454.

33 H. Zeng, X.-W. Du, S. C. Singh, S. A. Kulinich, S. Yang, J. He and W. Cai, *Adv. Funct. Mater.*, 2012, **22**, 1333–1353.

34 Z. Yan and D. B. Chrisey, *J. Photochem. Photobiol. C : Photochem. Rev.*, 2012, **13**, 204 – 223.

35 S. Barcikowski and G. Compagnini, *Phys. Chem. Chem. Phys.*, 2013, **15**, 3022–3026.

36 V. Amendola and M. Meneghetti, *Phys. Chem. Chem. Phys.*, 2013, **15**, 3027–3046.

37 D. Amans, M. Diouf, J. Lam, G. Ledoux and C. Dujardin, *J. Colloid. Interface Sci.*, 2017, **489**, 114–125.

38 D. Zhang, B. Gökce and S. Barcikowski, *Chem. Rev.*, 2017, **117**, 3990–4103.

39 J. Xiao, P. Liu, C. X. Wang and G. W. Yang, *Prog. Mater. Sci.*, 2017, **87**, 140–220.

40 D. Zhang, J. Liu, P. Li, Z. Tian and C. Liang, *ChemNanoMat*, 2017, **3**, 512–533.

41 J. Zhang, M. Chaker and D. Ma, *J. Colloid Interface Sci.*, 2017, **489**, 138–149.

42 A. Kanitz, M.-R. Kalus, E. L. Gurevich, A. Ostendorf, S. Barcikowski and D. Amans, *Plasma Sources Sci. Technol.*, 2019, **28**, 103001.

43 R. Streubel, G. Bendt and B. Goekce, *Nanotechnology*, 2016, **27**, 205602.

44 R. Streubel, S. Barcikowski and B. Goekce, *Opt. Lett.*, 2016, **41**, 1486–1489.

45 STREM Chemicals, Inc. (USA) and the i-Colloid in-house branch of IMRA America, Inc. (USA) (see `http://nano.imra.com/`) sell nanoparticles produced by pulsed laser ablation in liquids. STREM Chemicals is the distributor of Particular GmbH (see `http://particular.eu/start.html`). Nara Machinery Co. LTD sells Laser Ablation system which can performed PLAL synthesis (see `http://www.nara-m.co.jp/english/product/particle/las.html`).

46 I. Martial, F. Balembois, J. Didierjean and P. Georges, *Opt. Express*, 2011, **19**, 11667.

47 J. Bárta, M. Pospížil and V. Čuba, *J. Radioanal. Nucl. Chem.*, 2010, **286**, 611–618.

48 T. Gbur, V. Čuba, V. Múčka, M. Nikl, K. Knížek, M. Pospížil and I. Jakubec, *J. Nanopart. Res.*, 2011, **13**, 4529–4537.

49 J. Bárta, M. Pospížil and V. Čuba, *Mater. Res. Bull.*, 2014, **49**, 633–639.

50 J. Bárta, L. Procházková, V. Vaněček, M. Kuzár and V. Nikl, M.and Čuba, *Appl. Surf. Sci.*, 2019, **479**, 506–511.

51 V. Čuba, L. Procházková, J. Bárta, A. Vondrášková, T. Pavelková, E. Mihóková, V. Jary and M. Nikl, *J. Nanopart. Res.*, 2014, **16**, 2686.

52 L. Procházková, T. Gbur, V. Čuba, V. Jarý and M. Nikl, *Opt. Mater.*, 2015, **47**, 67–71.

53 V. Perebeinos, S. Chan and F. Zhang, *Solid State Commun.*, 2002, **123**, 295–297.

54 F. Zhang, P. Wang, J. Koberstein, S. Khalid and S. Chan, *Surf. Sci.*, 2004, **563**, 74–82.

55 W. H. Weber, K. C. Hass and J. R. McBride, *Phys. Rev. B*, 1993, **48**, 178–185.

56 I. Kosacki, V. Petrovsky, H. U. Anderson and P. Colomban, *J. Am. Ceram. Soc.*, 2002, **85**, 2646–2650.

57 Z. Wu, M. Li, J. Howe, H. M. Meyer, III and S. H. Overbury, *Langmuir*, 2010, **26**, 16595–16606.

58 S. Agarwal, X. Zhu, E. J. M. Hensen, B. L. Mojet and L. Lefferts, *J. Phys. Chem. C*, 2015, **119**, 12423–12433.

59 Z. Wu, A. K. P. Mann, M. Li and S. H. Overbury, *J. Phys. Chem. C*, 2015, **119**, 7340–7350.

60 G. N. Vayssilov, M. Mihaylov, P. St Petkov, K. I. Hadjiivanov and K. M. Neyman, *J. Phys. Chem. C*, 2011, **115**, 23435–23454.

61 S. Jendrzej, B. Goekce, M. Epple and S. Barcikowski, *ChemPhysChem*, 2017, **18**, 1012–1019.